Journal of Nuclear Materials 441 (2013) 674–680

Contents lists available at SciVerse ScienceDirect

Journal of Nuclear Materials

journal homepage: www.elsevier.com/locate/jnucmat

Study of irradiated mod.9Cr–1Mo steel by synchrotron extended X-ray absorption fine structure

Meimei Li [a,*], Dan Olive [b], Yulia Trenikhina [b], Hasitha Ganegoda [b], Jeff Terry [b], Stuart A. Maloy [c]

[a] Argonne National Laboratory, 9700 South Cass Avenue, Argonne, IL 60439-4838, United States
[b] Illinois Institute of Technology, 3101 South Dearborn, Chicago, IL 60616, United States
[c] Los Alamos National Laboratory, MST-8, MS-H816, Los Alamos, NM 87545, United States

ARTICLE INFO

Article history:
Available online 12 October 2012

ABSTRACT

Synchrotron extended X-ray absorption fine structure (EXAFS) spectroscopy measurements were performed to study the dose dependence of and alloying effects on irradiation-induced changes in the local atomic environments in a mod.9Cr–1Mo ferritic-martensitic steel. The measurements were carried out at room temperature on non-irradiated and irradiated specimens exposed to 1, 4, and 10 displacement per atom (dpa) at 40–70 °C. The EXAFS data for Fe, Cr, Mo, and Nb K-edges were recorded, and the local structure close to the X-ray absorbing atom was determined. Irradiation caused significant reductions in peak amplitude in the Fe, Mo and Nb K-edge Fourier transformed EXAFS. The data showed a systematic decrease in coordination number of neighbor atoms with increasing irradiation dose, and the dose dependence of the coordination loss was dependent on the specific element. The measured damage around Fe sites can be correlated with the dpa value, while the loss of near neighbors around Mo saturated at ~1 dpa. The coordination in the Fe matrix was reduced less by irradiation than either the coordination of Mo in solution or Nb in carbides. It was demonstrated that EXAFS can provide a detailed, atomic level description of radiation damage in complex alloy systems.

1. Introduction

Ferritic–martensitic steels are the lead structural materials for various types of advanced fission and fusion energy systems. These alloys have excellent resistance to irradiation-induced swelling, good thermal properties, and low cost. Modified 9Cr–1Mo ferritic–martensitic steel is a prime candidate for structural applications in advanced sodium-cooled fast reactors [1]. Mod.9Cr–1Mo is a Fe-9%Cr–1%Mo steel modified with addition of V and Nb. The high temperature strength of mod.9Cr–1Mo relies on tempered martensite stabilized by $M_{23}C_6$ carbides and a fine distribution of vanadium/niobium carbon-nitride (MX) precipitates; molybdenum in the solution contributes to the strength through solid solution strengthening [2]. Irradiation can significantly change the initial optimum microstructure and degrade the mechanical performance of the alloy. A previous electron microscopy study on specimens of mod.9Cr–1Mo irradiated by mixed high-energy protons and neutrons showed that irradiation at low temperatures produces a large number of dislocation loops, carbide amorphization, and/or nanocrystallinity [3]. For such a complex alloy a variety of advanced characterization tools are required to fully understand irradiation defect production and accumulation and irradiation-induced/enhanced precipitation or dissolution processes.

The use of X-ray scattering and X-ray absorption spectroscopy has provided valuable insight into radiation damage in nuclear materials [4,5]. Extended X-ray absorption fine structure (EXAFS) spectroscopy has been used to probe irradiation-induced changes of local atomic environments in several classes of alloys, e.g. dilute Al alloys, steels, zirconium alloys, etc. [6–15]. The EXAFS oscillations of the X-ray absorption spectrum begin approximately 40 eV above the absorption edge and continue to higher photon energy. The oscillations arise from the interference of the outgoing photoelectrons with the scattered waves from neighboring atoms. The measurements of the oscillations can probe the local atomic environment of the absorbing atom, providing chemically-specific, local structural parameters such as atom types, coordination number and position of neighboring atoms. The element-specific nature of the technique makes it particularly useful for study of complex alloy systems [16]. EXAFS was employed to investigate interstitial-solute interactions in electron-irradiated dilute Al(Zn) and Al(Ag) [6,7]. It was demonstrated that the EXAFS is a useful tool to probe detailed structure of interstitial-solute complexes and to study defect trapping and detrapping reactions. Edwards et al. [8] characterized thermally-aged and neutron-irradiated Fe–Cu and

* Corresponding author. Tel.: +1 630 252 5111.
E-mail address: mli@anl.gov (M. Li).

0022-3115/$ - see front matter © 2012 Elsevier B.V. All rights reserved.
http://dx.doi.org/10.1016/j.jnucmat.2012.09.039

Fe–Cu–Ni model alloys by EXAFS, and found that Cu atoms were not completely incorporated into "fcc-like" precipitates even after long-term aging; Ni remained in solid solution, prohibiting Cu precipitation. The mean Cu environments in neutron-irradiated binary and tertiary model alloys were essentially the same. The EXAFS technique has also been applied to study the atomic-level damage around Fe, Cu, Ni, and Mn atoms in neutron-irradiated reactor pressure vessel steels [9,10]. Vacancy type defect environments were found to form in close proximity to Cu, Ni, and Mn solute atoms, but no apparent structural changes around Fe. Recent studies on ion-irradiated PM2000 oxide-dispersion-strengthened steel by the EXAFS showed no major changes of yttria particles after irradiation at low temperatures to low doses, but clear structural changes after irradiation at high temperature [11–13].

Despite the great potential of synchrotron radiation techniques, the application to the investigation of irradiated materials is still in their infancy. The availability of ultra-brilliant 3rd-generation synchrotron X-ray sources, improved optics, and detector technologies has stimulated new interest in structure determination in irradiated materials using the EXAFS. This study was to explore the detailed structural changes of irradiation defects at specific alloying elements using EXAFS and to understand the role of alloying elements in defect structural evolution during irradiation in a class of ferritic–martensitic steel. Synchrotron EXAFS measurements were conducted on non-irradiated and irradiated specimens of mod.9Cr1-Mo exposed to 1, 4, and 10 dpa at 40–70 °C. The EXAFS data at the Fe, Cr, Mo, and Nb K-edges were obtained. The local structure close to the X-ray absorbing atom was determined from the EXAFS data. The information on the near neighbors of the absorbing atoms allowed us to follow the defect structural evolution during irradiation at the atomic scale with statistic significance.

2. Experimental procedure

The material examined was mod.9Cr–1Mo, an archive material available for post-irradiation examination in the Advanced Test Reactor National Scientific User Facility (ATR NSUF) Pre-irradiated Sample Library. The chemical composition of the alloy (in weight percent), was 9.24 Cr, 0.96 Mo, 0.21 V, 0.054 Nb, 0.089 C, 0.035 N, 0.002 Al, 0.08 Cu, 0.47 Mn, 0.16 Ni, 0.021 P, 0.006 S, 0.28 Si, 0.002 Ti, 0.019 Co, 0.01 W, 0.008 O, bal. Fe. The alloy was normalized at 1038 °C for 1 h and air-cooled, and then tempered at 760 °C for 1 h and air-cooled to room temperature prior to irradiation.

The mod.9Cr–1Mo steel was irradiated in the 800 MeV, 1 mA proton beam at the Los Alamos Neutron Science Center (LANSCE). Details of the irradiation experiments are given in the references [17–19]. Specimens chosen for synchrotron radiation experiments were irradiated to the following three conditions: (1) 1 dpa, 45 appm He, 645 appm H at 40 °C, (2) 4 dpa, 273 appm He, 2600 appm H at 47 °C, and (3) 10 dpa, 697 appm He, 6200 appm H at 69 °C. Note that He and H were produced in the samples due to the high energy proton beam. Specimens were coupons with width 2 mm, thickness 250 μm, and length 8 mm. The highest activity of specimens was 10 mR/h beta plus gamma at a distance of 30 cm. To reduce the specimen activity for safe handling, coupon specimens were cut into smaller pieces with a reduced length. All non-irradiated and irradiated specimens were then individually mounted in a triple-contained aluminum sample holder (Boojum Scientific) sealed with kapton tape (see Fig. 1) in the Irradiated Materials Laboratory at Argonne National Laboratory (ANL). The assembled specimen had activity <5 mR/h beta plus gamma and <1 mR/h gamma at 30 cm, and no removable contamination. The triple-contained specimens were then transferred to the ANL Advanced Photon Source (APS) for synchrotron radiation experiments.

The X-ray absorption experiments on non-irradiated and irradiated specimens were performed at the APS Materials Research Collaborative Access Team (MRCAT) beamline 10-ID. The beamline is equipped with a Si (1 1 1) monochromator consisting of a cryo-cooled first crystal and a 250 mm long second crystal, providing an energy range of 4.8–30 keV with the first harmonic. The absorption spectra of the mod.9Cr–1Mo steel were recorded at the Fe, Cr, Mo, and Nb K-edges in the fluorescence geometry at room temperature. The self-absorption effects were corrected prior to analysis.

3. Results

Figs. 2–4 show the normalized Fe K-edge absorption spectra, k^2-weighted EXAFS data ($k^2\,\chi(k)$) and their Fourier transformations in real space ($\chi(R)$), respectively, for non-irradiated specimens and specimens irradiated to 1, 4, and 10 dpa. k is the wave number of the photo-electron, and $\chi(k)$ is the oscillations as a function of photo-electron wave number. Systematic changes with increasing irradiation doses are evident in the $\chi(R)$. Marked attenuations occurred for all peaks following irradiations, indicative of loss of coordination around the absorbing Fe atom. The intensity of peak maxima decreased continuously as the irradiation dose increased.

Figs. 5 and 6 show the normalized Mo K-edge absorption spectra and the $\chi(R)$ data, respectively, for the mod.9Cr–1Mo non-irradiated specimens and specimens irradiated to 1, 4, and 10 dpa. The local atomic structure around the Mo absorber was similar before and after irradiations except for reduced coordination after irradiation. The drop of peak intensity is evident at 1 dpa, and no further significant changes were observed as irradiation doses increased.

Figs. 7 and 8 show the normalized Nb K-edge absorption spectra and the Fourier transformed EXAFS data, respectively, for the mod.9Cr–1Mo non-irradiated specimens and specimens irradiated to 1, 4, and 10 dpa. In contrast to the Fe and Mo K-edge data, the Nb K-edge data showed minor differences in peak positions and shapes, particularly in the higher-level shells, in addition to the changes in peak amplitudes in the Fourier transformation profiles

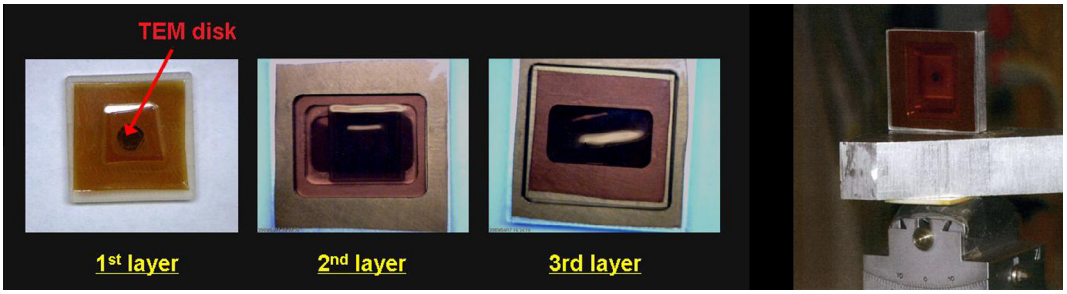

Fig. 1. The specimen loaded in a triple-contained aluminum sample holder sealed with kapton tape for EXAFS measurements.

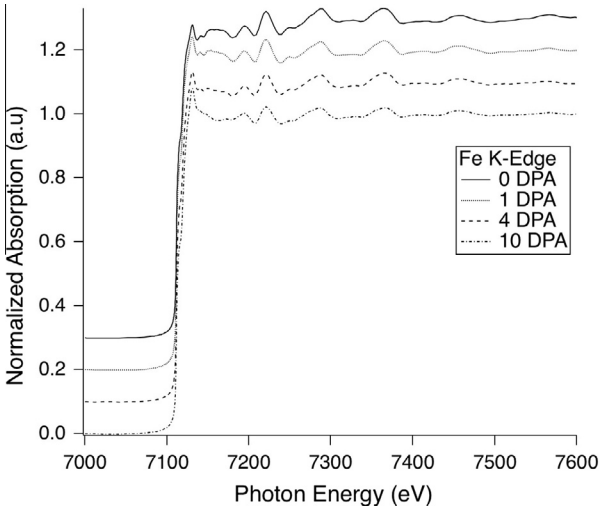

Fig. 2. The normalized Fe K-edge absorption spectra for non-irradiated specimen and irradiated specimens of mod.9Cr–1Mo.

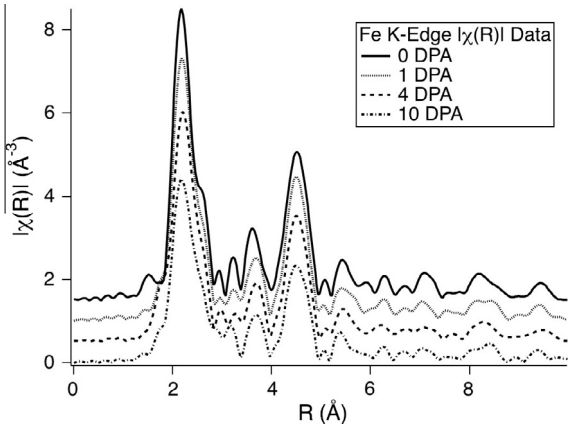

Fig. 4. The Fourier transformations of the Fe K-edge EXAFS for non-irradiated specimen and irradiated specimens of mod.9Cr–1Mo.

after irradiations. The amplitudes of all peaks were reduced by irradiation.

The Fourier transformed Cr K-edge EXAFS data for the mod.9Cr–1Mo non-irradiated specimens and specimens irradiated to 1 and 10 dpa are shown in Fig. 9. The Cr K-edge data showed evident evolution during irradiation, particularly at higher doses. These changes may possibly indicate structural changes in Cr-carbides. Detailed analysis of the Cr K-edge absorption spectra is being conducted, and will be reported in future publications.

Table 1 summarizes the optimized structural parameters around the absorbing atoms, Fe, Mo, and Nb, including interatomic distance, R, Debye–Waller factor, σ^2, and coordination number, N, derived from the fits of the EXAFS peaks. The EXAFS near-neighbor modeling included both single scattering paths and multiple scattering paths. The EXAFS Fe and Mo K-edge data shows characteristics of the body-centered-cubic (bcc) Fe lattice structure. The analysis using the bcc Fe lattice model gives rise to a good fit for both Fe and Mo K-edge data. Theoretically, the bcc Fe has eight nearest-neighbors at a distance of 2.47 Å, and six next-nearest neighbors at 2.86 Å, which contribute to the first peak in the Fourier transformed EXAFS profile. The third neighbor shell has 12 atoms at 4.05 Å shown by the second peak, and the fourth neighbor shell has 24 atoms at 4.74 Å shown by the third peak. The multiple scattering paths give 48 neighbor atoms at a distance of 3.91 Å and 16 atoms at 4.95 Å. Note that the Fourier transformed EXAFS data in Figs. 4, 6, 8 and 9 are not corrected for scattering phase shifts, so the peak positions were shifted to lower radial distances than the true bond distances. The fitted values of the interatomic distance around Fe sites are close to the theoretical values, with differences <2%. The deviation from the mean value is no more than 0.03 Å. The fitted interatomic distances around Mo sites are larger than those in the bcc Fe lattice model for all near-neighbor shells. The deviation of the interatomic distance from the mean values is <1%. The fits to the EXAFS data of the irradiated specimens showed irradiation-induced structural changes primarily in the coordination number.

The coordination number around the Fe absorbing atom is plotted as a function of dose in Fig. 10a, and the coordination number, normalized to the coordination number of the non-irradiated specimen, is plotted in Fig. 10b as a function of dose. Note that only single scattering paths were included in Fig. 10. Focusing on single scattering paths, irradiation to 1 dpa reduced the coordination number of neighboring atoms in the 1st and 2nd shells, but not in the 3rd and 4th shells. This is a nonphysical result, but the higher shells have significant multiple scattering contributions which

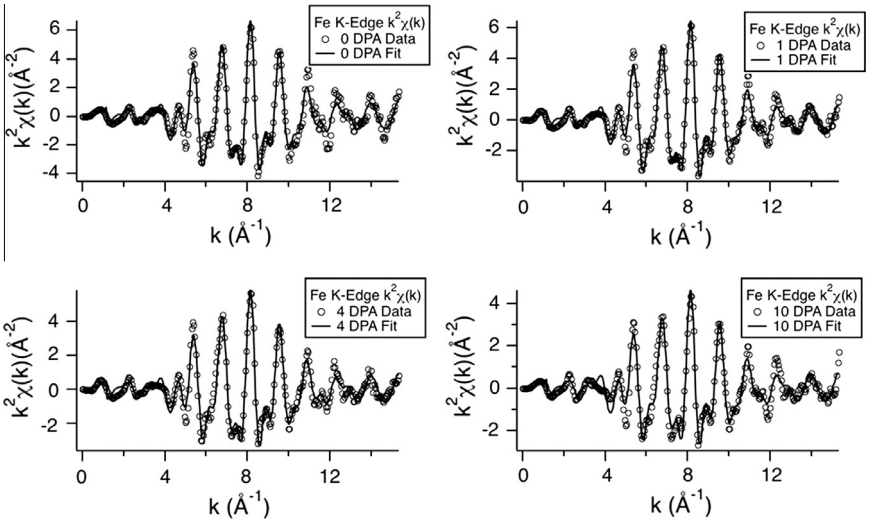

Fig. 3. The K^2-weighted Fe K-edge EXAFS data for non-irradiated specimen and irradiated specimens of mod.9Cr–1Mo.

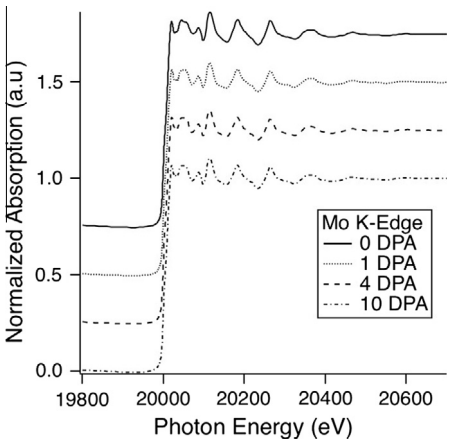

Fig. 5. The normalized Mo K-edge absorption spectra for non-irradiated specimen and irradiated specimens of mod.9Cr–1Mo.

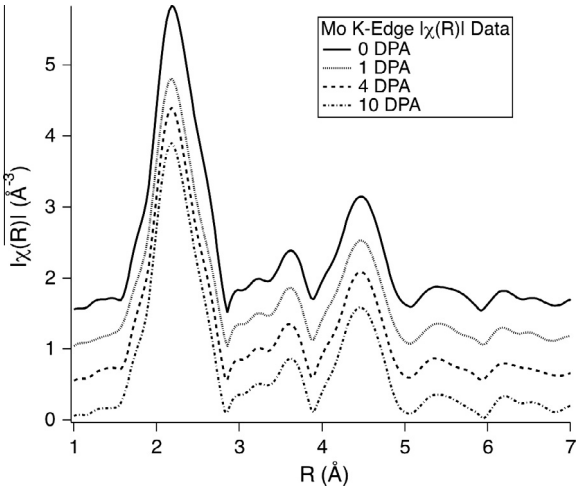

Fig. 6. The Fourier transformations of the Mo K-edge EXAFS for non-irradiated specimen and irradiated specimens of mod.9Cr–1Mo.

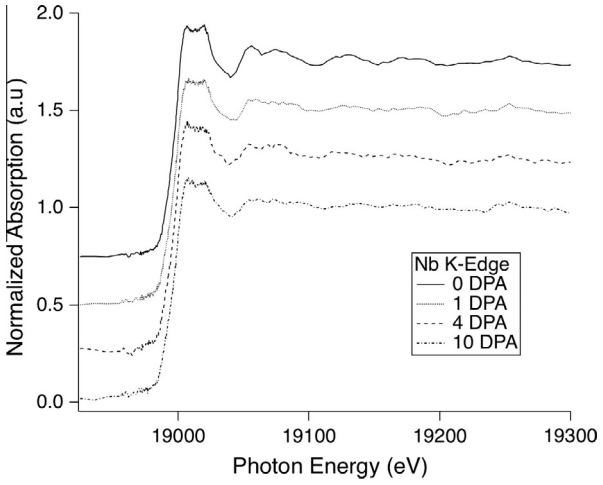

Fig. 7. The normalized Nb K-edge absorption spectra for non-irradiated specimen and irradiated specimens of mod.9Cr–1Mo.

complicates the analysis. Further analysis of how the multiple scattering paths affect the interpretation is ongoing. Irradiation to higher doses (4 and 10 dpa) reduced the coordination number of

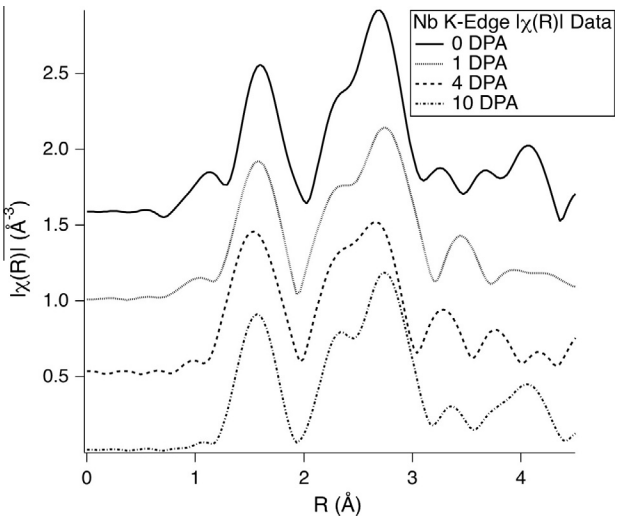

Fig. 8. The Fourier transformations of the Nb K-edge EXAFS for non-irradiated specimen and irradiated specimens of mod.9Cr–1Mo.

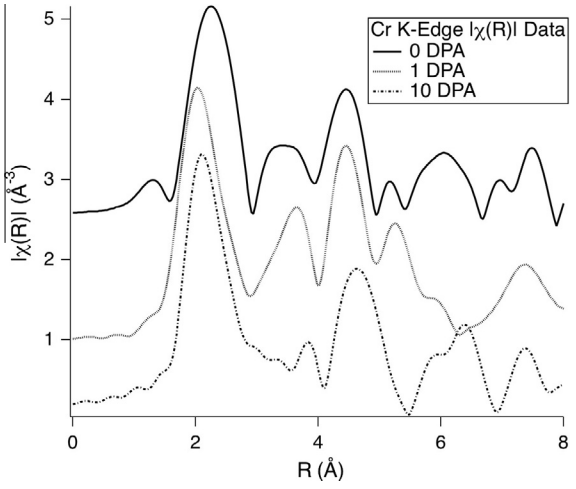

Fig. 9. The Fourier transformations of the Cr K-edge EXAFS for non-irradiated specimen and irradiated specimens of mod.9Cr–1Mo.

neighboring atoms in all the first four shells. The loss of the coordination number is nearly 30% at 10 dpa. The loss of coordination number around Fe follows a nearly linear relationship with irradiation dose, with an average loss rate of 3%/dpa.

The atomic environment around Mo before and after irradiation is shown in Fig. 11, where the coordination number as a function of dose is given in Fig. 11a, and the normalized coordination number as a function of dose in Fig. 11b. Again, only single scattering paths were included in Fig. 11. Irradiation to 1 dpa reduced the coordination number of neighboring atoms dramatically. The loss of coordination number saturated at ~1 dpa. Irradiation to higher doses (4 and 10 dpa) caused no further reductions in number of near neighbor atoms. Again focusing on single scattering, the maximum loss of the coordination number around Mo at 1 dpa is ~25% in the first shell, ~10% in the second shell, and became even smaller in the third and fourth shells. As with Fe, further analysis of how the multiple scattering paths affect the interpretation is ongoing.

The Nb K-edge data showed the structure of the NbC compound. Irradiations did not introduce significant changes in peak positions and shapes, particularly in the first and second shells around Nb. The reductions in peak amplitudes in irradiated

Table 1
Summary of structural parameters around absorbing atoms, Fe, Mo and Nb for non-irradiated and irradiated specimens.

Path	R (Å) model	R (Å) fit	σ^2 (Å^2)	N model	N (0 dpa) fit	N (1 dpa) fit	N (4 dpa) fit	N (10 dpa) fit
Fe K-edge fitting results								
Fe	2.47	2.47 ± 0.01	0.003 ± 0.002	8	8.1 ± 1	7.8 ± 1	6.8 ± 1	5.6 ± 1.5
Fe	2.86	2.85 ± 0.01	0.003 ± 0.002	6	5.5 ± 1.5	5.3 ± 1.5	5.3 ± 1.5	3.8 ± 2
Fe	4.05	4.05 ± 0.03	0.007 ± 0.002	12	16.4 ± 6	16.6 ± 6	14.9 ± 6	12.6 ± 7
Fe	4.74	4.74 ± 0.02	0.013 ± 0.002	24	25.6 ± 6	25.9 ± 5	21.3 ± 5	17.9 ± 8
Fe–Fe	4.95	5.03 ± 0.02	0.005 ± 0.002	16	13.6 ± 4	12 ± 4	12 ± 4	8.9 ± 5
R factor					0.037	0.024	0.026	0.063
Mo K-edge fitting results								
Fe	2.47	2.51 ± 0.03	0.003 ± 0.001	8	7.7 ± 1	6.9 ± 1	7.0 ± 1	7 ± 1
Fe	2.86	2.89 ± 0.03	0.003 ± 0.001	6	5.9 ± 1	4.4 ± 1.5	4.6 ± 1.5	4.7 ± 1.5
Fe–Fe	3.91	3.96 ± 0.04	0.003 ± 0.005	48	45 ± 2	30 ± 2.5	32 ± 2.5	33 ± 2.5
Fe	4.05	4.08 ± 0.03	0.006 ± 0.002	12	9.5 ± 3	9.5 ± 3	8.9 ± 5	9.4 ± 5
Fe	4.74	4.81 ± 0.02	0.008 ± 0.002	24	32.4 ± 8	31.4 ± 8	32 ± 8	32.5 ± 8
Fe–Fe	4.95	5.09 ± 0.05	0.008 ± 0.002	16	9.4 ± 4	8.0 ± 4	8.3 ± 4	8.6 ± 4
R factor					0.012	0.027	0.029	0.026
Nb K-edge fitting results								
C	2.24	2.18 ± 0.04	0.005 ± 0.004	6	6.2 ± 1.5	4.8 ± 2.5	5.3 ± 3	4.0 ± 3
Nb	3.16	3.16 ± 0.03	0.008 ± 0.002	12	11.8 ± 3	8.9 ± 4	7.3 ± 4	6.8 ± 4
Nb–C	3.82	3.79 ± 0.04	0.009 ± 0.003	48	49 ± 5	29 ± 7	26 ± 7	18 ± 7
R factor					0.17	0.2	0.22	0.34

Note: "Fe–Fe" and "Nb–C" represent multiple scattering paths.

specimens were primarily due to the decrease in coordination number of neighbor atoms. The single scattering paths around Nb sites are surrounded by 6 C atoms at 2.18 ± 0.04 Å (compared to the model value, 2.24 Å) and 12 Nb atoms at 3.16 ± 0.03 Å (compared to the model value, 3.16 Å). The multiple scattering paths have 48 C atoms at 3.79 ± 0.04 Å (compared to the model value, 3.82 Å). The fitting parameters agree well with the model values. The coordination number of Nb sites as a function of dose is given in Fig. 12a, and the normalized coordination number as a function of dose in Fig. 12b. Irradiation to 1 dpa reduced the coordination number of neighboring atoms in all near neighbor shells. In contrast to the matrix damage around Fe and Mo, reductions in the coordination number are the smallest in the first C shell, followed by the second Nb shell, and the third C shell. The maximum loss of coordination number is ~40% at 1 dpa. Irradiation to higher doses (4 and 10 dpa) further reduced the coordination number of neighboring atoms, but to a lesser extent, and the first shells showed a similar loss rate above 1 dpa. The maximum loss of coordination number is ~60% at 10 dpa.

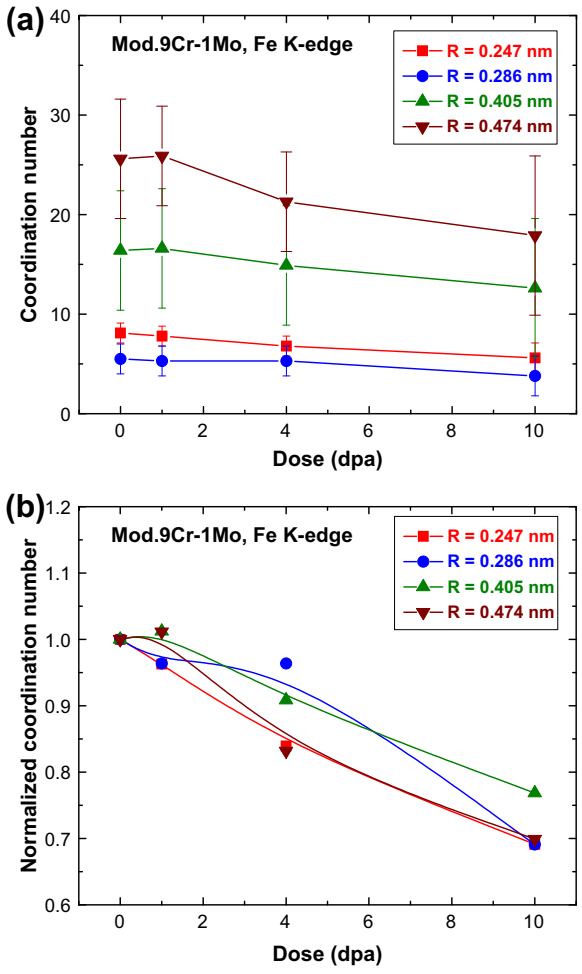

Fig. 10. The atomic environment around Fe before and after irradiation: (a) the coordination number and (b) the normalized coordination number, normalized to the coordination number in the non-irradiated specimen, as a function of dose for non-irradiated specimen and irradiated specimens of mod.9Cr–1Mo.

4. Discussion

Irradiation leads to the formation of a large population of interstitial and vacancy point defects or defect clusters. Radiation defects have been characterized primarily by electron microscopy in concert with other analytical tools. EXAFS has unique advantages in defect characterization due to its element-specific, local atomistic structural nature. The EXAFS probes atomic environments within the range of about 0.6 nm, providing detailed structural description of defects around a specific atom with statistic significance [20]. The EXAFS measurements of irradiated mod.9Cr–1Mo specimens in this study showed the sensitivity of the technique for various levels of irradiation doses. The reductions in peak amplitudes in the Fourier transformed EXAFS data were evident in all irradiated specimens, and the fits to the EXAFS data showed a systematic decrease in coordination number of neighbor atoms in irradiated specimens. Comparing the local atomic structure of the Fe and Mo atoms, irradiations continuously reduced the coordination numbers in the near-neighbor shells around Fe with increasing dose, and the measured damage of the Fe sites can be correlated with the dpa value, while the loss of near neighbors around Mo saturated at ~1 dpa. The first and second shells in metallic alloys are generally more sensitive to irradiation-induced local structural changes. The reductions in near-neighbor peak amplitudes were also observed in a neutron-irradiated reactor pressure vessel steel [9,10]. Post-irradiation annealing of neu-

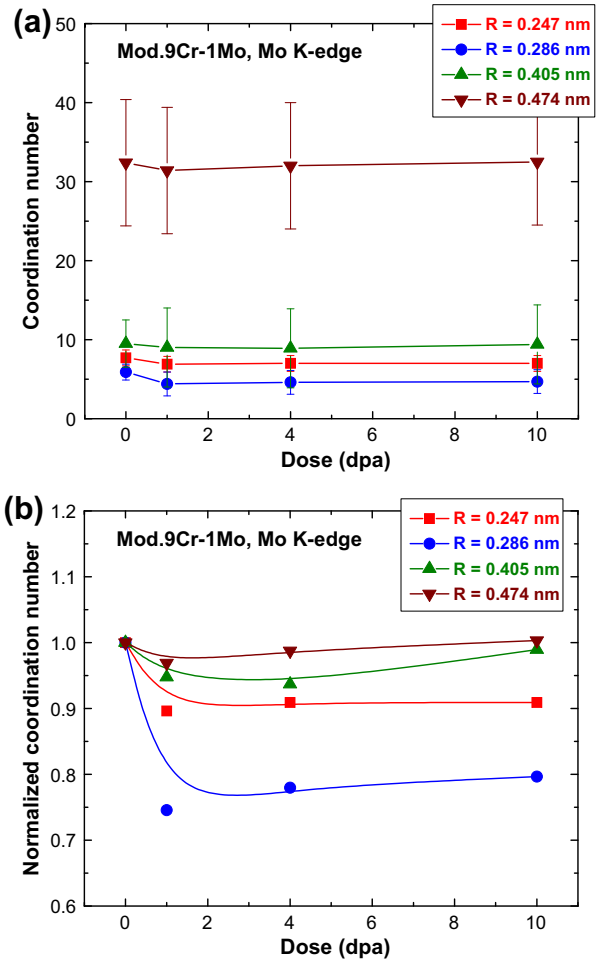

Fig. 11. The atomic environment around Mo before and after irradiation: (a) the coordination number and (b) the normalized coordination number as a function of dose for non-irradiated specimen and irradiated specimens of mod.9Cr–1Mo.

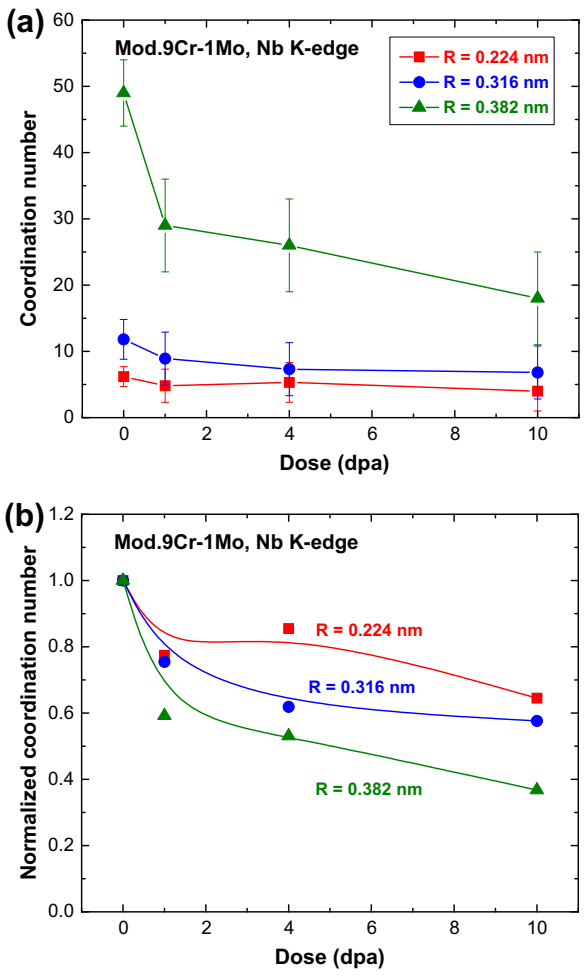

Fig. 12. The atomic environment around Nb before and after irradiation: (a) the coordination number and (b) the normalized coordination number as a function of dose for non-irradiated specimen and irradiated specimens of mod.9Cr–1Mo.

tron-irradiated specimens of the reactor pressure vessel steel increased the coordination numbers of near-neighbor atoms, approaching values close to that of non-irradiated material.

The Fe and Mo K-edge data demonstrated the matrix damage in irradiated specimens. The Nb K-edge data showed the structure of NbC, and provided information of microstructural changes of NbC precipitates due to irradiation. The NbC precipitates in mod.9Cr–1Mo steel give rise to high creep resistance, and their stability during irradiation is critical for maintaining superior mechanical performance in reactor environments. The EXAFS measurements showed that the peak positions and shapes, particularly the first and second shells around Nb were relatively unchanged after irradiations, indicating stable structure of the precipitate particles. The decrease of the peak maxima and corresponding loss of coordination number of near neighbors of the Nb environment implied strong defect trapping in NbC particles, and the effects were more pronounced in the higher-level shells, opposite to the damage around solute atoms.

A reduction in coordination number in irradiated specimens implies that there was a progressive increase in the number of vacancies around absorbing atoms during irradiation, as was observed in a neutron-irradiated reactor pressure vessel steel [9,10]. Irradiation of the mod.9Cr–1Mo steel with the high energy proton beam at LANSCE produced not only displacement damage but also an appreciable amount of helium and hydrogen. The concentration of helium and hydrogen was as high as 697 appm He and 6200 appm H in the 10-dpa irradiated specimen. Due to the extremely low solubility of helium in metals, helium diffuses easily through the lattice and can become trapped in vacancy sites. Helium bubbles are formed through nucleation and growth processes at high temperatures. A previous electron microscopy study on the same irradiated material did not find cavity (bubble and/or void) formation in specimens irradiated up to 10 dpa and at the highest gas levels [3]. The loss of coordination number around Fe, Mo, and Nb in the irradiated mod.9Cr–1Mo cannot confirm or rule out trapping of helium or hydrogen atoms in vacancy sites. EXAFS measurements of irradiated specimens annealed at various temperatures will provide further insight into vacancy or helium/hydrogen environments around the alloying elements.

Understanding the role of alloying elements on defect production and accumulation is important for the development of radiation-tolerant materials. It is known that alloying elements, either in solid solution or precipitates, have a significant effect on microstructural and microchemical evolution during irradiation in alloys and steels [21]. This study has demonstrated that the effect of alloying on defect evolution during irradiation can be assessed at the atomic level by the EXAFS. Three-dimensional vacancy-type defects are often examined by positron annihilation spectroscopy [22]. The EXAFS study of mod.9Cr–1Mo steel showed that EXAFS measurements not only detected local vacancy environments, but also provided chemically-specific distribution of vacancy defects and their structural information. It was clearly shown that vacancy (or He/H) environments were formed around major metallic elements, Fe, Mo, and Nb in the irradiated mod.9Cr–1Mo, and the

evolution of vacancy (or He/H) environments with increasing dose was element-dependent. The reduction in coordination number around Fe approached ~30% at 10 dpa, while the coordination number was reduced by ~25% around Mo, and ~40% around Nb even at ~1 dpa. Note that the calculated atomic radius of Nb is 1.98 Å, Mo 1.90 Å and Fe 1.55 Å, respectively [23]. For irradiation at 40–70 °C, both interstitials and vacancies are mobile in mod.9Cr–1Mo. It is apparent that oversized Mo and Nb atoms trapped vacancies more effectively than the Fe atoms, and the interactions between these alloying elements and vacancies were more active at lower doses. The effect of atomic size on interactions between alloying atoms and point defects has been well recognized. For instance, in austenitic Fe–Cr–Ni alloys, undersized impurity atoms interact preferably with interstitial defects, while oversized atoms interact with vacancies [24–27]. Depending on the distribution of alloying elements, either in solution or in precipitates, vacancy distribution around a probe atom varied in irradiated mod.9Cr–1Mo steel. The chemical-specific distribution of vacancies can have significant implication in the kinetics of vacancy type defect evolution. The information of vacancy environments formed around the major metallic elements may provide new insight into the design of new alloys resistant to irradiation-induced embrittelement, void swelling, helium embrittelement, and irradiation-induced segregation.

5. Conclusions

Synchrotron EXAFS measurements were performed at room temperature to study the dose dependence and alloying effects on local structural changes in mod.9Cr–1Mo ferritic–martensitic steel irradiated to 1, 4, and 10 dpa at 40–70 °C. Irradiation caused significant reductions in peak amplitude in the Fe, Mo and Nb K-edge Fourier transformed EXAFS in all irradiated specimens. Analysis of the EXAFS data showed the systematic loss in coordination numbers of neighbor atoms with increasing irradiation doses. The local atomic structure around Fe, Mo, Nb, and Cr was affected by irradiation in different fashion, which revealed the effect of alloying elements on defect evolution. The reduction in coordination number around Fe approached ~30% at 10 dpa, while the coordination number was reduced by ~25% around Mo and ~40% around Nb irradiated to as low as 1 dpa. The coordination number loss around Mo saturated at 1 dpa, while the loss of near neighbor around Fe atoms continued with increasing dose, and the measured damage can be correlated with the dpa values. It was demonstrated that EXAFS can provide a detailed, atomic level description of radiation damage in complex material systems.

Acknowledgements

The authors would like to thank Michael C. Billone, Yiren Chen, Jakub P. Dobrzynski Loren A. Knoblich, at the Irradiated Materials Laboratory, Brent A. Finney at Special Materials, Frederick A. Monette, Christopher G. Kolb, Nathan J. Duff, John H. Vacca, Stephen Butala, Health Physics, ESQ, at the Argonne National Laboratory; and Toby Romero and shipping/receiving staff at the Los Alamos National Laboratory. Work supported by the U.S. Department of Energy, Office of Nuclear Energy under Contract DE-AC02-06CH11357. A portion of this research was supported by the U.S. Department of Energy, Office of Nuclear Energy under DOE Idaho Operations Office Contract DE-AC07-051D14517.

References

[1] K. Natesan, Meimei Li, O.K. Chopra, S. Majamdar, J. Nucl. Mater. 392 (2009) 243.
[2] R.L. Klueh, D.R. Harries, High-Chromium Ferritic and Martensitic Steels for Nuclear Applications, ASTM International, 2001.
[3] B.H. Sencer, F.A. Garner, D.S. Gelles, G.M. Bond, S.A. Maloy, J. Nucl. Mater. 307–311 (2002) 266.
[4] P. Ehrart, J. Nucl. Mater. 216 (1994) 170.
[5] A. Froideval, M. Samaras, R. Iglesias, M.A. Pouchon, et al., Adv. Eng. Mater. 11 (2009) 459.
[6] T. Bolze, J. Peisl, Z. Phy. B – Condens. Matter 62 (1985) 9.
[7] W. Weber, J. Peisl, Phy. Rev. B 28 (1983) 28.
[8] A.B. Edwards, K.J. Roberts, S. Pizzini, W.J. Phythian, Philos. Mag. A 79 (1999) 1295.
[9] G. Kuri, S. Cammelli, C. Degueldre, J. Bertsch, D. Gavillet, J. Nucl. Mater. 385 (2009) 312.
[10] S. Cammelli, C. Degueldre, G. Kuri, J. Bertsch, D. Lutzenkirchen-Hecht, R. Frahm, J. Nucl. Mater. 385 (2009) 319.
[11] C. Degueldre, S. Conradson, W. Hoffelner, Comput. Mater. Sci. 33 (2005) 3.
[12] M.A. Pouchon, A.J. Kropf, A. Froideval, C. Degueldre, W. Hoffelner, J. Nucl. Mater. 362 (2007) 253.
[13] M.A. Pouchon, J. Chen, C. Dugueldre, A. Froideval, H. Emerich, W.V. Beek, Mater. Sci. Forum 561–565 (2007) 1761.
[14] C. Degueldre, S. Conradson, A. Amato, E. Campitelli, J. Nucl. Mater. 352 (2006) 126.
[15] A. Froideval, S. Abolhassani, D. Gavillet, D. Grolimund, C. Borca, J. Krbanjevic, C. Degueldre, J. Nucl. Mater. 385 (2009) 346.
[16] S.J. Gurman, J. Mater. Sci. 17 (1982) 1541.
[17] S.A. Maloy, W.F. Sommer, R.D. Brown, J.E. Roberts, J. Eddleman, E. Zimmerman, G. Willcutt, Progress report on the accelerator production of tritium materials irradiation program, in: M.S. Wechler, L.K. Mansur, C.L. Snead, W.F. Sommer (Eds.), Proceedings of the Symposium on Materials for Spallation Neutron Sources, TMS, Warrendale, PA, 1998, p. 35.
[18] M.R. James, S.A. Maloy, W.F. Sommer, P.D. Ferguson, M.M. Fowler, K. Corzine, in: 2nd International Topical Meeting on Nuclear Applications of Accelerator Technology, Gatlinburg, TN, 20–23 September, 1998, p. 605.
[19] G.J. Willcutt, S.A. Maloy, M.R. James, J. Teague, D.A. Siebe, W.F. Sommer, P.D. Ferguson, in: 2nd International Topical Meeting on Nuclear Applications of Accelerator Technology, Gatlinburg, TN, 20–23 September, 1998, p. 254.
[20] D.C. Koeningsberger, R. Prins, X-Ray Absorption: Principles, Applications, Techniques of EXAFS, SEXAFS and XANES, Wiley, 1988.
[21] P.R. Okamoto, L.E. Rehn, J. Nucl. Mater. 83 (1979) 2.
[22] M. Eldrup, Meimei Li, L.L. Snead, S.J. Zinkle, Nucl. Instrum. Methods B 266 (2008) 3602.
[23] E. Clementi, D.L. Raimondi, W.P. Reinhardt, J. Chem. Phys. 47 (1967) 1300.
[24] H. Watanabe, H. Aoki, T. Muroga, N. Yoshida, J. Nucl. Mater. 179–181 (1991) 529.
[25] V.L. Arbuzov, A.P. Druzhkov, S.E. Danilov, J. Nucl. Mater. 295 (2001) 273.
[26] A.P. Druzhkov, V.L. Arbuzov, D.A. Perminov, J. Nucl. Mater. 341 (2005) 153.
[27] H. Watanabe, T. Muroga, N. Yoshida, J. Nucl. Mater. 239 (1996) 95.